

ELECTRONIC SUPPLEMENT

VEDRAN LEKIĆ AND KAREN M. FISCHER

This supplement contains a detailed description of the array-picking algorithm and modified extended time multi-taper method that we used to obtain the constraints on lithospheric structure. Furthermore, it contains comparisons of the results obtained with and without the array-based picker, as well as those obtained using different subsets of data. Finally, it presents an analysis of uncertainties associated with the determination of LAB depths and strengths in this study, and explains the bootstrapping procedure that we used to quantify them.

1. ARRAY-BASED PICKING PROCEDURE

We modify the automatic data picking algorithm developed by *Abt et al.* (2010) to take advantage of dense seismic arrays present in the Western United States. Due to their focus on single-station stacking, *Abt et al.* (2010) used an automatic algorithm (henceforth AP1) based on signal-to-noise ratios in moving time-windows to identify the P and S arrival times on vertical and transverse component waveforms, respectively, observed at an individual station. AP1 is unreliable when noise levels are high; therefore, we typically apply it only on waveforms with estimated signal-to-noise ratios ≥ 2 . Yet, while this restriction eliminates the least reliable P and S picks, it greatly reduces the number of waveforms for which a P or S arrival-time is available. Furthermore, AP1 is not guaranteed to accurately pick the P and S arrival times even when the estimated signal-to-noise ratios are ≥ 2 , especially for S waves, which arrive during the P coda. In Figure 1, we show the histogram of the deviations of AP1-picked P (top) and S (bottom) arrival times from the predictions of ak135 (*Kennett et al.*, 1995). Note both the broad distribution, which suggests that the travel time picks are affected by noise, and the large peak in the distribution at zero, which results from reverting to the ak135 arrival time when signal-to-noise ratios in an individual waveform falls below 2.

Because the waveform of a single teleseismic body wave does not typically vary greatly across a dense seismic array, recordings from multiple spatially proximal stations can be aligned and stacked to yield a single, average waveform with lower noise levels. By modifying the AP1 algorithm to operate on this average waveform, the performance of the signal-to-noise based method can be improved dramatically.

We start with the waveforms of an earthquake recorded at a single station; waveforms of that same earthquake recorded at stations located closer than a threshold value of 10° are then identified. For picking P arrivals, the vertical component recording is used; the transverse component is used for picking S arrivals. A template waveform is then defined by the trimmed-mean of the recorded waveforms, with the extreme 10% of the

data discarded from the low and high ends. Then, cross-correlation is calculated between the individual recordings and the template waveform, windowed to be non-zero only within 5s of the predicted P arrival time and 15s of the predicted S arrival times. These cross-correlations are used to determine the time-shifts needed for optimal alignment of the individual waveforms to the template waveform, and also set the timing of the template waveform relative to the timing at the station in question. Since this template waveform has a substantially lower noise level than the constituent individual waveforms, the AP1 algorithm is run on this record. The relative P or S arrival times obtained by this method are then adjusted based on the cross-correlation time-shift between the master record and the waveform of the station-event pair of interest.

The question arises as to what P and S travel-time deviations Δt_P and Δt_S to associate with those earthquakes that are observed at a given station, but not recorded by multiple nearby stations. We choose to deal with this circumstance by constructing an interpolation function based on the set of observed $\Delta t_{P,S}$ - obtained via the array-picking scheme - and assign to each backazimuth and ray parameter a $\Delta t_{P,S}$. The interpolation function is a built-in MATLAB implementation of natural neighbor interpolation.

Figure S1 shows scatterplots of travel-time deviations Δt_P (left) and Δt_S (center) obtained with the AP1 algorithm against those produced by our array-based algorithm. When successful, the two methods produce consistent picks - note that the majority of the $\Delta t_{P,S}$ fall on the one-to-one line (black). However, the halo of Δt_S spanning the allowable range of travel time deviations seen with the AP1 algorithm but not seen with the array-based one demonstrates that AP1 is substantially more prone to random deviation than the array-based method. The fact that array-based P and S arrival picks are less affected by noise can also be inferred from the tighter distributions of $\Delta t_{P,S}$ in the histograms shown in the right panels of Figure S1.

The relative performance of the AP1 and array-based algorithms is also apparent in the comparison of the scatterplots of Δt_P versus Δt_S shown in Figure S2. Travel-time anomalies of S waves are typically ~ 2 times larger than those of P waves. Yet, while very clear in the array-based scatterplot (Figure S2b and c), this relationship is barely visible in the plot obtained by the AP1 algorithm (Figure S2a). The trend of the Δt_P versus Δt_S does not pass through the origin because the P and S waves have different travel-time offsets when analyzed with the new picking algorithm. This offset can result from differences in the V_p/V_s ratio between the regional mantle and the reference (ak135) model, and has implications for the relative deviations of V_p and V_s from the reference structure. Of particular importance is the streak apparent in Figure S2a, which corresponds to the thousands of waveforms whose signal-to-noise ratios were too low for the AP1 algorithm to estimate an S arrival. The absence of this streak in the array-based results (Figure S2b and c), demonstrates that the array-based algorithm has the added advantage of yielding a larger number of arrival-time estimates than is possible with AP1.

In Figure S3 we plot the average and standard deviation of Δt_S for all events observed at each individual station. The mean station Δt_S should reflect the average velocity difference between the crust and upper mantle structure beneath the station and that of the reference model ak135, which also implies that nearby stations should have similar mean Δt_S . With

respect to both these characteristics of reliable arrival picks, the array-based algorithm outperforms AP1. For one, the regional trend of faster Vs beneath the Colorado Plateau, the Wyoming Craton, and the Great Plains Craton to the east and slower Vs beneath the northern Great Basin and the southern Basin and Range is more clear in the map of mean station Δt_S obtained using the array-based algorithm. Furthermore, the standard deviation of Δt_S for all events observed at an individual station is substantially smaller when the array-based algorithm is used.

2. DECONVOLUTION

The deconvolution of S waveforms from the P waveforms is accomplished for each pair of P and SV waveforms using a MATLAB implementation of the extended-time (*Helffrich, 2006*) multiple-taper correlation method (*Park and Levin, 2000*). Unlike *Helffrich (2006)*, we follow the recommendation of *Shibutani et al. (2008)* and adopt a time-bandwidth product of 4 and a moving window length of 50 s, though we use 7 instead of 3 Slepian tapers and overlap moving time windows by 90%. The total length of our data windows is 100 seconds, as in *Abt et al. (2010)*. We choose to use large overlap in order to compensate for the degradation of signal at longer delay times that results from the reduced spectral resolution associated with using a higher time-bandwidth product. If we denote by $u_{P,SV}(t_n)$ the P or SV waveform in the n^{th} moving time window, where a window t_0 corresponding to $n = 0$ is centered on the S arrival in the case of Sp receiver functions, then the frequency-domain Sp receiver function $RF_n(\omega)$ corresponding to time window n is obtained by:

$$(1) \quad RF_n(\omega) = \frac{\sum_{k=1}^7 \mathcal{F}[Y^k(t_0)u_{SV}(t_0)]^* \mathcal{F}[Y^k(t_n)u_P(t_n)]}{\sum_{k=1}^7 \mathcal{F}[Y^k(t_0)u_{SV}(t_0)]^* \mathcal{F}[Y^k(t_0)u_{SV}(t_0)] + \lambda^2},$$

where \mathcal{F} denotes the Fourier Transform, and $Y^k(t_n)$ is the k^{th} Slepian taper spanning t_n . The time-domain receiver function $RF(t)$ is obtained by an inverse Fourier Transform followed by averaging across times sampled by multiple moving windows. The damping parameter λ is chosen to minimize the sum of the receiver function size and misfit between the observed daughter component and that predicted by the convolution of RF with P, both calculated with the L-1 norm.

3. EFFECTS OF THE ARRAY-BASED PICKING ALGORITHM

Do the improvements in the accuracy of P and S onset times translate into a more reliable 3D model of crustal and mantle discontinuities? In order to quantitatively answer this question, we compare the variance σ^2 of the receiver functions (RF) - obtained with the two auto-picking techniques - contributing to the value of the CCP stack at every (r_k, θ_k, ϕ_k) . If we have N receiver functions contributing to the value of the CCP stack at a location (r_k, θ_k, ϕ_k) , and their weights in the CCP stack are given by w_i , the variance is given by:

$$(2) \quad \sigma_k^2 = \frac{1}{N-1} \sum_i^N \left(RF_{i,k} - \frac{1}{N} \sum_i^N RF_{i,k} \right)^2$$

Then, in Figure S4, we plot the distributions of the σ^2 at a set of depths. With a single exception (at 60 km depth), the RFs obtained with the array-based picking algorithm are more coherent (smaller variances), indicating that the array-based algorithm outperforms the AP1 algorithm, especially at greater depths, which are important for robustly constraining lithospheric structure. The substantial reduction in variance among the receiver functions going into the CCP stack obtained with the array-based algorithm suggests that the improved picking accuracy improves the coherence and reliability of the CCP stacks.

Does the decreased variance of the RFs that contribute to each voxel in the CCP stacks yield more easily interpretable images? To answer this question, in Figure S5 we plot vertical slices through the CCP stacks constructed using the AP1 algorithm and those constructed using the array-based algorithm. For example, a strong negative Sp arrival (blue) appears to be generated across the base of the lithosphere in the southern Basin and Range (profile H) in the CCP stack obtained with the improved phase-picking and deconvolution approaches; this remarkable feature is washed out and barely visible in the CCP stacks constructed with the AP1 algorithm. Further to the north (profile J), the new methods yield a prominent negative Sp arrival that extends beneath the Great Basin, abruptly weakening beneath the Wyoming Craton. This behavior is much less clear with the AP1 algorithm. We attribute the larger and more coherent negative Sp arrivals obtained with the array-based algorithm to more accurate phase windowing and a reduction in waveform scatter.

4. EFFECTS OF THE TRANSPORTABLE ARRAY

How well-suited are the station spacing and length of deployment of the Transportable Array (TA) for constraining lithospheric structure using CCP stacking of Sp receiver functions? As a site of numerous temporary, dense seismic deployments, the western U.S. offers a variety of different lithospheric and crustal structure settings in which we can address this question through direct comparisons of CCP stacks obtained with and without the TA. In Figure S6, we show vertical sections through our 3D mantle discontinuity model that parallel the line of the broadband LARISTRA deployment (*Gao et al.*, 2004), which had an average station spacing of 18 km and a deployment duration of just under 2 years. We find that CCP stacks constructed with TA data by themselves (middle) show clear and coherent NVG phases across the region; in comparison, Sp CCP stacks constructed with temporary deployment data alone (top) show weaker and less coherent NVG phases. TA spacing appears to be dense enough to enable the retrieval of variations in Moho depth; on the other hand, it does not enable reliable imaging of intra-crustal discontinuities, which are only coherent and continuous in the CCP stacks supplemented with data from temporary deployments.

5. UNCERTAINTY ANALYSIS

In order to quantify the uncertainties in the CCP stacks due to random noise in the data and outliers, we carry out a bootstrapping analysis in which we generate and analyze 50

different datasets by resampling our actual dataset. We start by drawing, with replacement, N integers from a uniform distribution between 1 and N . The integers 1 to N are taken to represent the S_p receiver functions used to construct our stacks in the main text, so that a single resampled dataset consists of the set of N receiver functions identified by the N randomly drawn integers. Each randomly resampled dataset is analyzed in precisely the same way that the original dataset is analyzed, and a CCP stack is constructed. The process is repeated 50 times, yielding 50 different CCP stacks. Then, for each CCP stacks, we run the same automatic algorithm used in Figure 5 of the main text to determine the depths and amplitudes of the negative velocity gradient (NVG) phases, which may represent a seismically defined lithosphere-asthenosphere boundary (LAB) or mid-lithospheric discontinuities (MLD).

In Figure S7, we plot maps of the mean (top) and standard deviation (bottom) of the NVG phase depth and amplitude calculated for the 50 CCP stacks. The mean depth map (a) is very similar to the map for the actual dataset shown in Figure 5, confirming that the depths to the LAB/MLD phases are robustly constrained by our dataset, and are not the result of random errors and outliers. We note that the LAB phase remains shallow beneath the Great Basin, the Basin and Range, and is of intermediate depth beneath the High Rockies. The shallowing of the LAB phase from depths of 100–120 km in the northern and central Colorado Plateau to depths of 60–80 km along its margins is also clear. Deeper and more laterally-variable depths are once again seen beneath the Wyoming Basin, and the Great Plains craton.

Looking at the standard deviation of LAB/MLD depths (c), we see that beneath much of the Basin and Range, the Great Basin, and portions of the High Rockies, the uncertainty on the LAB/MLD depths is <5 km. However, very large apparent uncertainties are seen in localized areas, often associated either with the edges of the study region (e.g. Salton Trough) or with boundaries between regions with deep and shallow NVG phases (e.g. southeastern New Mexico). Nevertheless, it appears that there might be an association between areas with deeper-than-average MLD/LAB phases and uncertainty. Is this because the CCP stacks are highly variable in these regions, or because of small changes in relative amplitudes of multiple NVG phases that cause the automatic algorithm to jump around in a range of depths?

In Figure S8, we plot north-south vertical sections coincident with those shown in Figure 3 of the main text, but this time through the mean of the 50 CCP stacks. Then, to illustrate the variability across the CCP stacks, we blank out all regions where the mean amplitude of the stack is significant to less than 95%, that is, where its absolute amplitude is smaller than 2 standard deviations calculated across the 50 CCP stacks. The remarkable consistency between these sections and those shown in Figure 3 implies that the uncertainties in the LAB/MLD depths (Figure S7c) result from minor changes in the relative amplitudes of multiple NVG phases, rather than major differences between CCP stacks obtained with different random dataset realizations. Particularly clear is the first-order difference between the relatively shallow and large amplitude phases that we interpret as the seismically-defined LAB, and weaker, more distributed in depth phases that we observe beneath stable regions and interpret as the MLD.

As the vertical sections of Figure S8 suggest, the mean amplitude map (Figure S7b) is also highly consistent with the results obtained with the full dataset (Figure 5). In particular, the large-scale contrast in amplitude of the NVG phase —and, therefore, also in the velocity contrast and or depth range across which it is distributed —between regions that have undergone recent extension and/or magmatic activity and those that have remained relatively stable, remains clearly discernible in the mean amplitude map. The map of standard deviations associated with each of the amplitude estimates (Figure S7d) shows both that the amplitudes are not strongly affected by noise, and, more importantly, that the spatial distribution of the errors is uncorrelated with this large-scale contrast in LAB/MLD amplitudes. Interestingly, the streaks of very low amplitude uncertainties are seen beneath some of the temporary deployments (the LARISTRA line is particularly striking), suggesting that the dense temporary deployments can dramatically improve the reliability of amplitude recovery in Sp studies of lithospheric structure.

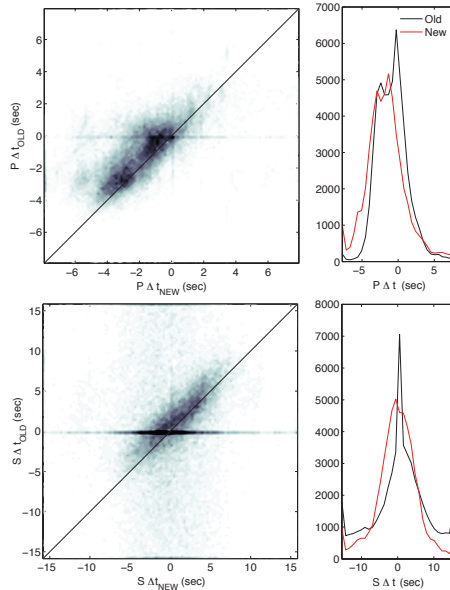


FIGURE 1. (left) Scatterplots of the travel time deviations from the predictions of ak135 (*Kennett et al.*, 1995) of P (top) and S (bottom) arrivals ($\Delta t_{P,S}$) obtained using the AP1 algorithm (*Abt et al.*, 2010) and the array-based picking algorithm described here. (right) Histograms of the $\Delta t_{P,S}$ obtained using the AP1 algorithm (black) and the array-based picking algorithm described here (red). The array-based picker produces much more reliable S picks, and can be applied to a much larger subset of the data, as indicated by the disappearance of the $\Delta t_S = 0$ peak, to which value the picking algorithm defaults when the signal-to-noise ratio is too low.

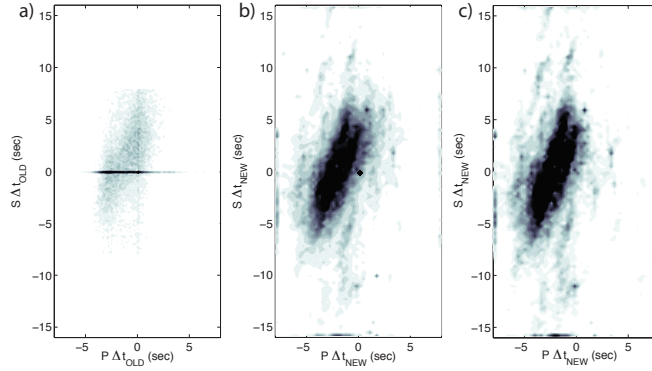


FIGURE 2. Scatterplots of the travel time deviations of P vs S arrivals ($\Delta t_{P,S}$) from the predictions of ak135 (Kennett *et al.*, 1995). (left) AP1 algorithm. (middle) Array-based picking algorithm presented in this paper. (right) Array-based algorithm applied only to stations of the Transportable Array.

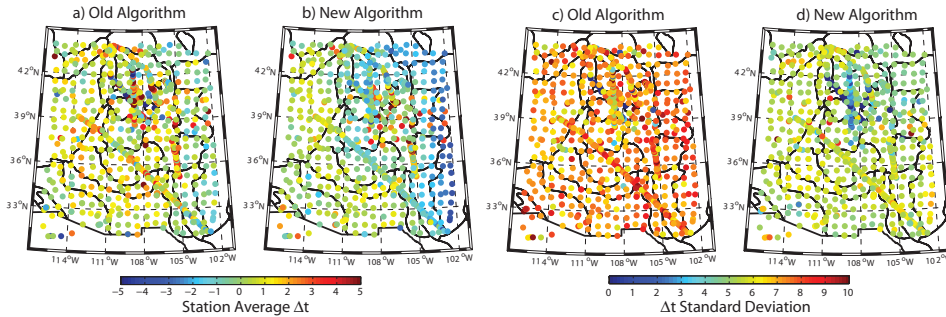


FIGURE 3. Station average S travel time deviations (Δt_S) from the predictions of ak135 obtained using the AP1 algorithm (a) and the array-based picking algorithm described here (b). Standard deviation of Δt_S for each station obtained using the automatic picking algorithm of Abt *et al.* (2010) (AP1) (c) and the array-based picking algorithm described here (d). Note the substantial reduction in the variance of picks for individual stations, and the systematically faster arrivals seen beneath the Colorado Plateau, the Wyoming Craton, and the tectonically stable eastern margins of the study region.

REFERENCES

- Abt, D., K. Fischer, S. French, H. Ford, H. Yuan, and B. Romanowicz (2010), North American lithospheric discontinuity structure imaged by Ps and Sp receiver functions, *J. geophys. Res.*, 115(B09301), doi:10.1029/2009JB006914.

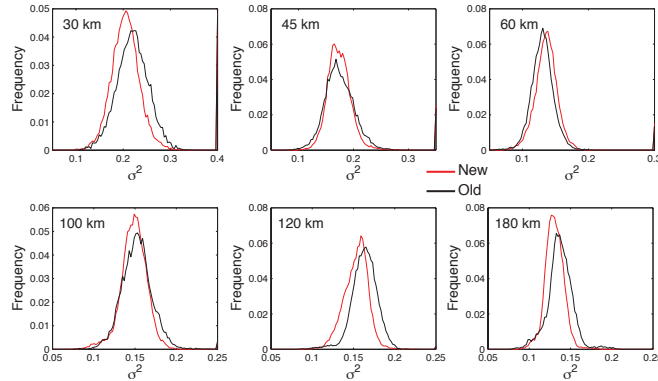


FIGURE 4. Histograms of the variance of receiver function values that go into constructing the the CCP stacks at 30, 45, 60, 100, 120 and 180 km depth. Receiver functions obtained using data picked with the AP1 algorithm (black) show higher variability than those obtained with the new algorithm (red), except at 60 km depth. Since all the other processing steps are identical, this behavior confirms that the use of the array-based picking algorithm yields more reliable receiver functions which sum more coherently during the CCP stacking procedure. Interestingly, this effect increases with depth, suggesting that the retrieval of deep structure is particularly enhanced by the use of the array-based picking algorithm.

- Gao, W., S. P. Grand, W. S. Baldrige, D. Wilson, M. West, J. F. Ni, and R. Aster (2004), Upper mantle convection beneath the central Rio Grande Rift imaged by P and S wave tomography, *Journal of Geophysical Research*, *109*, B03305, doi:10.1029/2003JB002743.
- Helffrich, G. (2006), Extended-time multitaper frequency domain cross-correlation receiver-function estimation, *Bulletin of the Seismological Society of America*, *96*(1), 344–347.
- Kennett, B., E. Engdahl, and R. Buland (1995), Constraints on seismic velocities in the Earth from traveltimes, *Geophysical Journal International*, *122*(1), 108–124.
- Lowry, A., and M. Pérez-Gussinyé (2011), The role of crustal quartz in controlling Cordilleran deformation, *Nature*, *471*(7338), 353–357.
- Park, J., and V. Levin (2000), Receiver functions from multiple-taper spectral correlation estimates, *Bulletin of the Seismological Society of America*, *90*(6), 1507–1520.
- Shibutani, T., T. Ueno, and K. Hirahara (2008), Improvement in the extended-time multitaper receiver function estimation technique, *Bulletin of the Seismological Society of America*, *98*(2), 812–816.

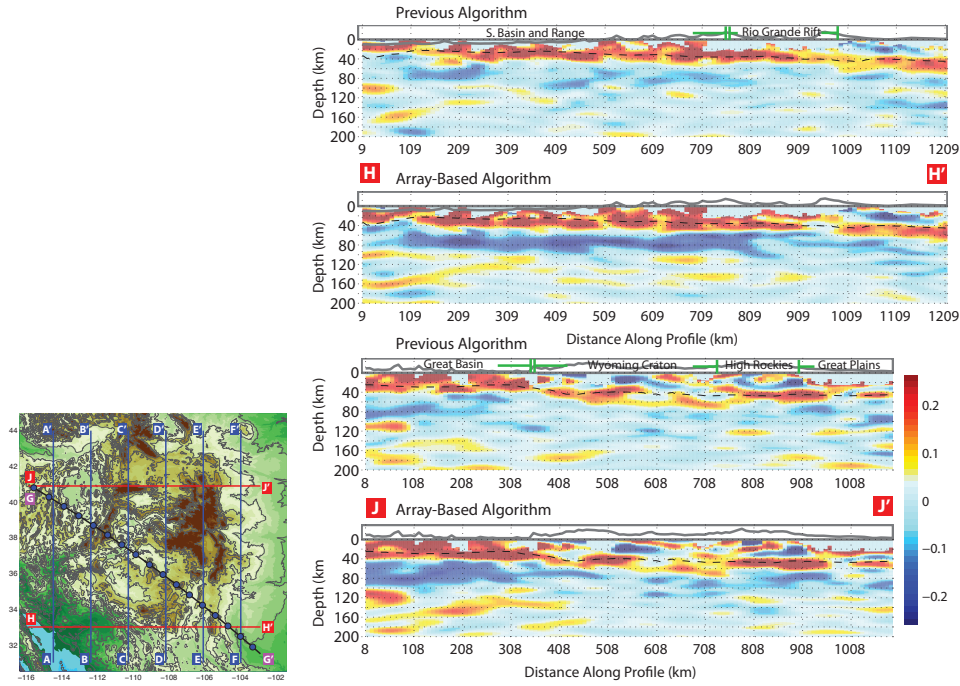


FIGURE 5. (left) Map showing the surface traces of the vertical sections plotted in this, and subsequent, figures. (right) Vertical sections through Sp CCP stacks obtained using the AP1 algorithm and the array-based one presented in this paper. Warm (cool) colors indicate velocity increase (decrease) with depth and topography (black line) is exaggerated 10-fold. The dashed line traces the Moho from *Lowry and Pérez-Gussinyé* (2011). Throughout the region of study, the array-based algorithm yields CCP stacks that show more laterally-coherent structures. While the positive Sp arrival associated with the Moho is visible regardless of the picking algorithm, deeper features are better imaged using the array-based picking algorithm.

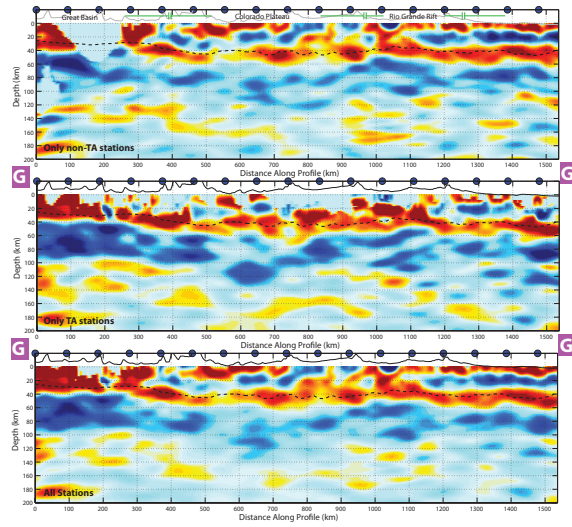


FIGURE 6. Vertical sections through our Sp CCP stacks constructed with the array-based picking algorithm using all stations (bottom), only the stations of the Transportable Array (middle), or all non-TA stations (top). The surface trace of the section parallels that of the LARISTRA deployment, as shown in Figure 5. Though the spacing of the TA does not allow for reliable imaging of intra-crustal discontinuities, it is adequate for constraining crustal thickness and lithospheric structure across the region. The longer deployment and high-quality installations of the TA also help to explain why the negative Sp arrival is clearer in the stacks with these data.

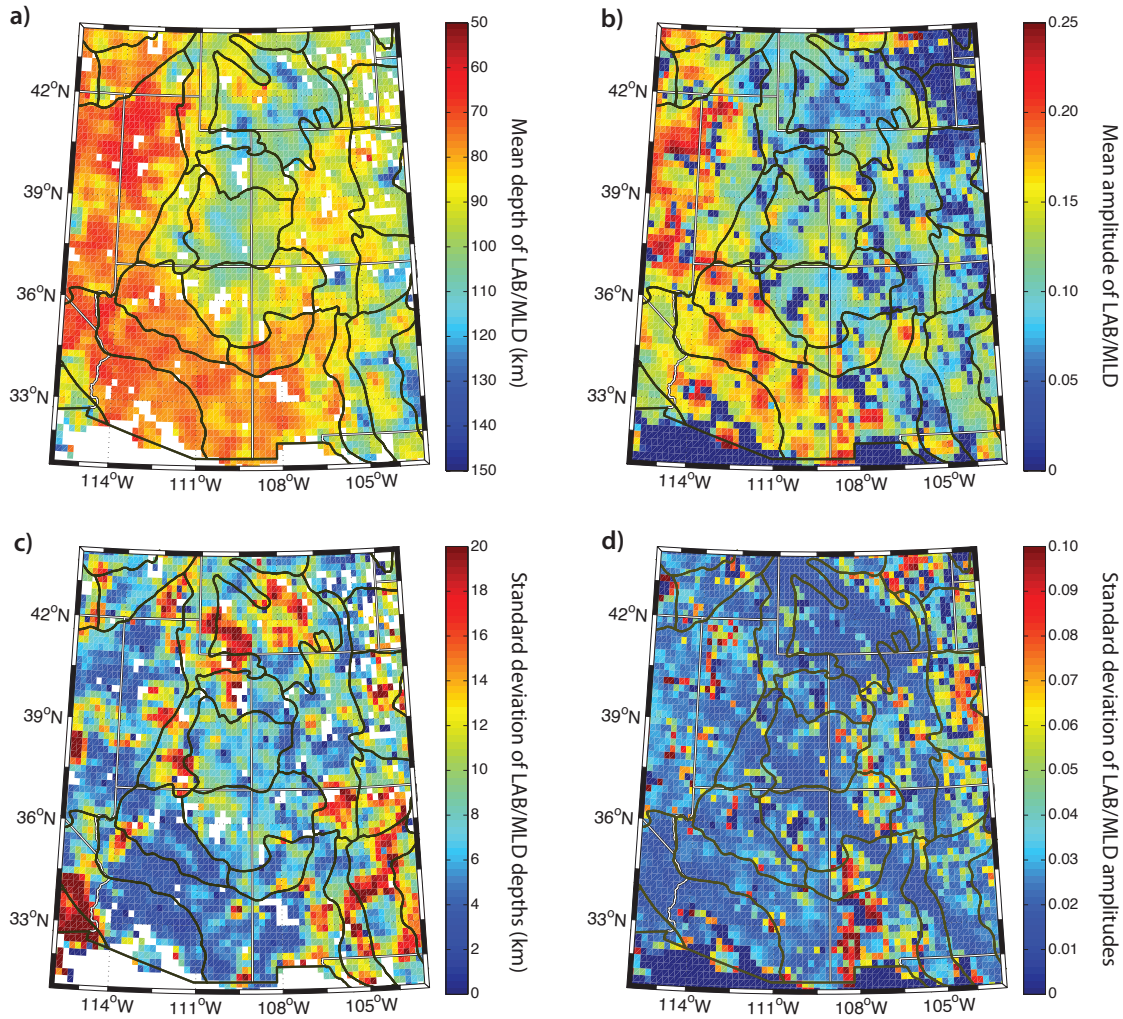


FIGURE 7. Maps of the mean depth (a), mean amplitude (b), standard deviation of depth (c) and standard deviation of amplitude (d) of the LAB/MLD phase observed in the common conversion point stacks calculated for 50 randomly resampled dataset realizations (bootstrap analysis). Note the similarity between the mean depth and amplitude maps and those obtained for the full dataset in Figure 5, confirming the robustness of the LAB/MLD depth and amplitude results discussed in the main text.

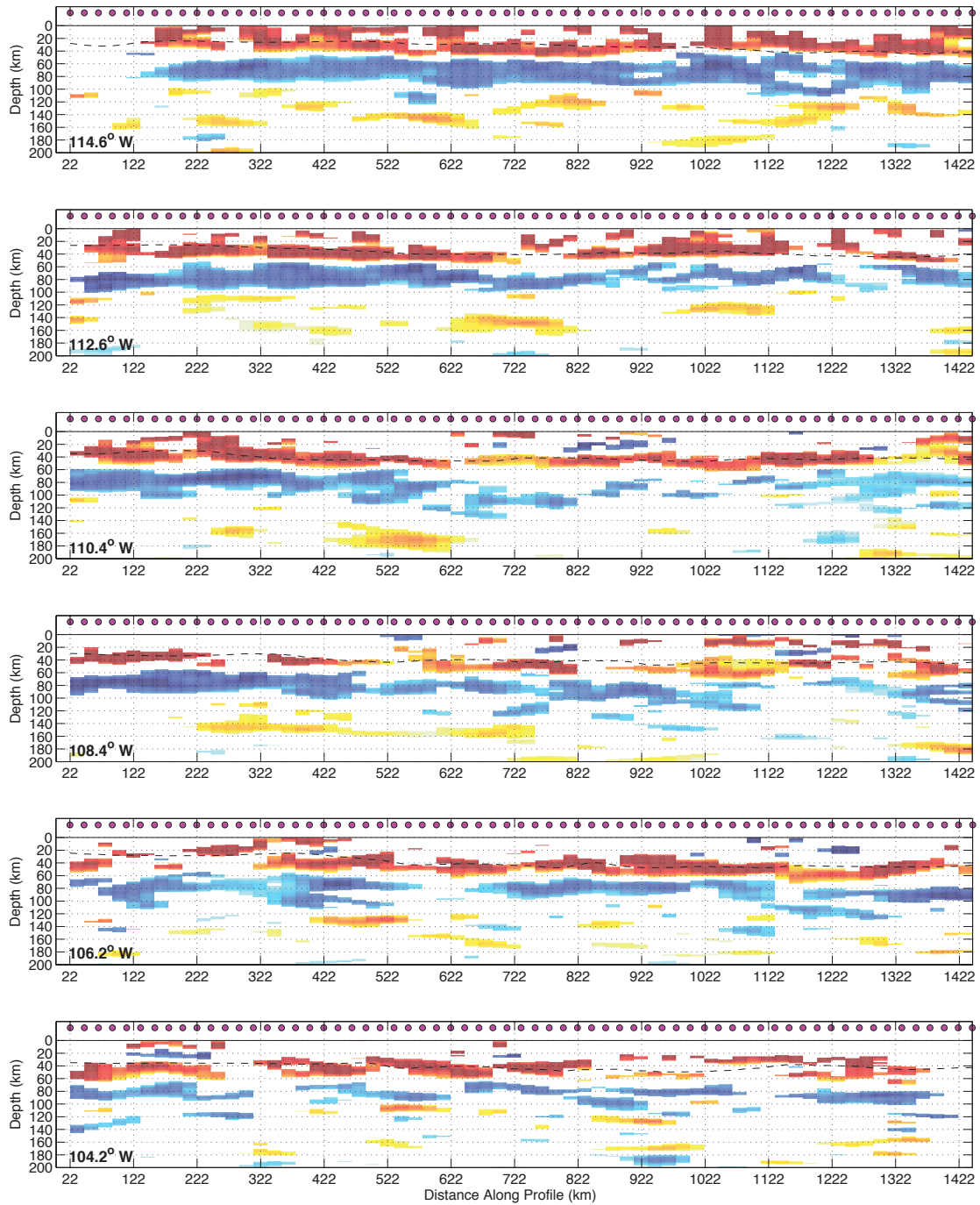


FIGURE 8. Vertical sections through the mean of the 50 Sp CCP stacks, spatially coincident with those shown in Figure 3 of the main text. Portions of the stacks that are significant to less than 95% confidence are whited out. Note the similarity between these vertical sections and those obtained with the full dataset (Figure 3), demonstrating that the features analyzed in the main text are reliably imaged.